



Diffusiophoresis-enhanced particle deposition for additive manufacturing

Samannoy Ghosh, Department of Mechanical Engineering, University of Utah, Salt Lake City, UT 84112, USA

Saebom Lee, School of Mechanical Engineering, Sungkyunkwan University, Suwon, Gyeonggi-do 16419, Republic of Korea

Marshall V. Johnson, Woodruff School of Mechanical Engineering, Georgia Institute of Technology, Atlanta, GA 30313, USA

James Hardin, Materials and Manufacturing Directorate, Air Force Research Laboratory, Wright-Patterson Air Force Base, Dayton, OH 45433, USA

Viet Sang Doan, and Sangwoo Shin, Department of Mechanical and Aerospace Engineering, University at Buffalo, The State University of New York, Buffalo, NY 14260, USA

Surya R. Kalidindi, Woodruff School of Mechanical Engineering, Georgia Institute of Technology, Atlanta, GA 30313, USA

Jinkee Lee, School of Mechanical Engineering, Sungkyunkwan University, Suwon, Gyeonggi-do 16419, Republic of Korea

Jesse T. Ault, Center for Fluid Dynamics, School of Engineering, Brown University, Providence, RI 02912, USA

Yong Lin Kong , Department of Mechanical Engineering, University of Utah, Salt Lake City, UT 84112, USA

Address all correspondence to Jesse T. Ault at jesse_ault@brown.edu and Yong Lin Kong at yong.kong@utah.edu

(Received 16 April 2023; accepted 1 August 2023; published online: 14 September 2023)

Abstract

The ability to govern particle assembly in an evaporative-driven additive manufacturing (AM) can realize multi-scale features fundamental to creating printed electronics. However, existing techniques remain challenging and often require templates or contaminating solutes. We explore the control of particle deposition in 3D-printed colloids by diffusiophoresis, a previously unexplored mechanism in multi-scale AM. Diffusiophoresis can introduce spontaneous phoretic particle motion by establishing local solute concentration gradients. We show that diffusiophoresis can play a dominant role in complex evaporative-driven particle assembly, enabling a fundamentally new and versatile control of particle deposition in a multi-scale AM process.

Introduction

The ability to control the deposition of colloids, such as nano-materials, with a 3D-printing process can impart, program, or modulate functional properties (e.g., mechanical,^[1] optical,^[2] electrical,^[2] thermal^[3]) in otherwise passive printed objects (henceforth called “multi-scale AM”). When integrated with extrusion-based AM,^[4] evaporative-driven assembly leverages multi-phase interactions between solutes, solvents, substrates, and the microenvironment to spontaneously control colloidal particles during the printing process. Owing to the highly sensitive nature of evaporative assembly, a broad range of multi-scale and hierarchical features (e.g., thin films^[5] to high-aspect-ratio colloidal structures^[6]) can be generated without the need for additional tools (e.g., lasers or acoustic systems), by modulating the ink and printing parameters. Indeed, the desired target patterns for AM can vary based on the target application. For example, a uniform thin film is required for printed electronic devices (such as LEDs),^[2] but nonuniform features, such as ring-like features, have been used to create novel transparent conductors.^[4]

However, the highly sensitive nature of evaporative assembly also leads to susceptibility to evaporation dynamic that leads to the creation of unintended features (i.e., defects). For example, it is challenging to consistently generate thin, uniform layers^[7] critical for printing active functional devices. Often, nonuniform patterns, including so-called “coffee-rings”^[8],

worm-like domains, cellular/lamellar structures, and sawtooth patterns, are frequently generated due to dynamic changes of the ink, substrate, or microenvironment.^[9]

Governing the evaporative-driven assembly can be achieved by modulating the multi-phase dynamics and soft matter physics. For example, Marangoni effects^[10,11] can be introduced via the addition of co-solvents, thermal gradients, or vapor concentrations. These induce recirculating flows that drive colloids from the contact line toward the drop center. In previous work, quantum dot (QD) solutions with a dichlorobenzene co-solvent^[2] produced microstructures with greater uniformity than those with pure toluene. “Coffee-ring” effects can be reduced by treating silicon and polydimethylsiloxane substrates with plasma to depin the contact line. Mechanical templates can also guide assembly or introduce confinement to modulate drying behaviors.^[4] However, these strategies introduce interfering parameters, such as changes in solution composition that alter the properties of the printed film or require additional templates and devices that limit potential applications and scalability for manufacturing practice.

One unexplored mechanism to achieve multi-scale AM is diffusiophoresis, which is the spontaneous phoretic motion of colloidal particles due to local solute concentration gradients and consists of chemiphoretic and electrophoretic contributions. Chemiphoresis is the motion of a particle due to the osmotic pressure gradient along the particle’s surface, and electrophoresis occurs with electrolyte solutes when the cations and anions have different diffusivities. In an electrolyte gradient, this difference spontaneously generates a local electric

Samannoy Ghosh and Saebom Lee are co-first authors.

field. As counter ions are attracted to the surface, a thin layer of charged fluid called the Debye layer is formed around the particle. This Debye layer is accelerated by the electric field, resulting in the motion of the particles. Chemiphoresis drives particles up the solute gradient, and electrophoresis may act in either direction. Derjaguin et al. introduced the concept of diffusioosmosis, where solute gradients induced slip over solid surfaces,^[12] and extended this to particle diffusiophoresis in electrolyte gradients.^[13] Anderson and Prieve showed that in a solute concentration gradient ∇c , the diffusiophoretic velocity of a particle is $u_{dp} = \Gamma_p \nabla \ln c$, where Γ_p is the diffusiophoretic mobility, a function of the particle's size, and zeta potential.^[14–16] This logarithmic dependence is the source of several particle behaviors facilitating control strategies such as banding/focusing^[17] and long-lived chemically driven effects. Additionally, a wide range of novel diffusiophoretic particle behaviors has been discovered, including banding, focusing, patterning, tuning of colloidal interactions, and enhanced particle transport.^[17,18]

While the theoretical understanding of diffusiophoresis is well established and applications in areas such as filtration, cleaning, and microfluidics have been demonstrated, the study of diffusiophoresis in AM has not been explored. Previous demonstrated applications with diffusiophoresis include microfluidic mechanisms for pre-concentrating DNA, focusing/spreading particle beams in junctions, segregation, and spatial patterning of particles, including λ -DNA,^[19] trapping under rectified gradients,^[20] enhanced transport in dead-end pores,^[17] techniques for measuring zeta potentials, filtration via CO₂-induced diffusiophoresis,^[21] cleaning by surfactant gradients and others. The unifying aspect of these is the introduction of solute gradients to a fluid/particle system to induce controlled particle dynamics. Indeed, recent research^[22] has demonstrated the use of non-contaminating solutes (e.g., soluble gases) as the driving force of diffusiophoresis to facilitate migration of particles. Such research suggests the potential to

incorporate diffusiophoresis as an active control strategy in AM systems. However, it remains an open question whether such techniques can generate sufficient forces to guide the complex particle assembly in multi-scale AM.

Here, we present simulations and experiments demonstrating the application of diffusiophoresis in an AM system. We developed a diffusiophoresis-enhanced microextrusion-based AM platform that leverages evaporative-driven printing inside a microenvironment to study the effect of non-contaminating solutes on the deposition dynamics. The integrated microenvironment chamber, with microextrusion printing and *in-situ* fluorescence imaging, is shown in Fig. 1. We modulate the concentration of soluble gases in the microenvironment to drive diffusiophoresis in drying droplets, and we image and characterize the deposition dynamics and final printed patterns. Significantly different patterns occur in N₂ and CO₂ environments, highlighting the impact of diffusiophoresis on the dynamics. We also performed simulations to gain insights into the effects of diffusiophoresis in the complex evaporation process. To our knowledge, the role of soluble gas-driven diffusiophoresis on sessile drop evaporation has not been considered. We simulate the diffusiophoretic transport of particles in non-evaporating and evaporating drops both with and without Marangoni effects, demonstrating the impact of diffusiophoresis on the particle motions when exposed to CO₂.

Materials and methods

Materials

Fluorescent amine-functionalized polystyrene (aPS) latex particles (diameter = 1 μ m, Sigma Aldrich) were suspended at a concentration of 2.5 mg/ml in distilled water. The particle size distribution and zeta potential were measured by dynamic light scattering (Mobius, Wyatt Technologies).

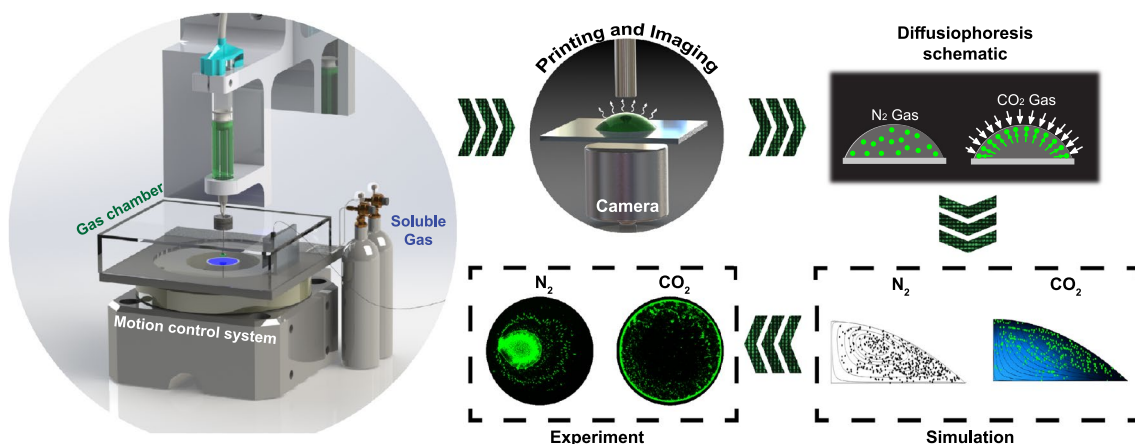


Figure 1. Schematic illustrations of the integrated printing/imaging platform to demonstrate diffusiophoresis in multi-scale AM. A customized chamber regulates the controlled flow of gases (N₂ and CO₂) inside the chamber and monitors the microenvironment parameters including humidity and temperature. The imaging platform captures real-time images of the depositions upon printing. Simulations provide insights into the physics and along with the experiments support the feasibility of the technique for multi-scale AM.

Printing

A micro-syringe pump was used to control the printing flow rate of the ink. The platform includes a four-axis micron-resolution motion control system (Aerotech, PA, USA) with translation and rotation capabilities for microscale precision in positioning and print speeds. We used $170 \pm 5 \mu\text{m}$ thick glass slides (Thorlabs, NJ, USA) as substrates, and drops were printed with 25-gauge needles (GA). Substrates were cleaned using acetone and isopropyl alcohol and dried using compressed N_2 prior to printing. The radii of printed drops were approximately 1.2 mm.

Imaging

Printed samples were imaged using inverted fluorescence microscopy (LEICA Microsystems, Germany) at $2.5 \times$ magnification with a monochrome FITC filter. Particles were visualized with green color using the LAS-X software to aid pattern visualization. Samples were imaged using two techniques. First, time-series images of the entire evaporation process were captured at constant exposure of 300 ms at 3-s intervals. Second, dried patterns were imaged at multiple exposures to obtain higher dynamic range. Thus, small, delicate features could be obtained at higher exposures while preserving spatial data from thicker features obtained at lower exposures. The imaging platform automatically captured the above-mentioned image sets using a custom Python code.

Microenvironment chamber

The custom-built microenvironment chamber was fabricated using a 3D-printed design structure (Form 3B, Formlabs) with a 1.6-mm-thick transparent acrylic bottom for imaging purposes. The top incorporates a septum, allowing the nozzle system to penetrate while minimizing gas leakage. Gas inlets and outlets were connected to valves to prevent leakage. The chamber integrates temperature, humidity, and CO_2 sensors to monitor the microenvironment. The gas introduced in the chamber was pumped through a desiccator unit to control the relative humidity inside the chamber.

Our custom microenvironment-chamber-printing platform can isolate the printing environment from ambient gases outside the chamber. This enables us to maintain a stable gas environment during the print and minimizes leakage of gases from the chamber. The primary control parameters for our experiments are the CO_2 and N_2 gas concentrations in the chamber. The humidity, temperature, and gas composition were constantly monitored throughout printing. We observed minimal gas concentration variation over the entire evaporation duration (~30 min). The CO_2 concentration was consistently maintained at 0.0% for the control experiments using N_2 . In the gaseous environment of CO_2 , the CO_2 concentration saturated and maintained a stable reading at $73 \pm 2\%$. The relative humidity was maintained below 30% throughout the evaporation process.

Image analysis

Image analysis was used to calculate the change in the area of printed drops through the drying process. Initial state images were captured immediately after deposition, and final state images were captured after drying. All the droplets were imaged at 300 ms exposure to provide good contrast between the drop and background. Boundaries of the printed drops were identified using canny edge detection. A morphological closing process was then used to create contiguously linked edges. The drop area was then segmented using a morphological filling operation. All steps, from edge detection to morphological filling, were conducted on both the initial and final state images. Although simple pixel counting works to calculate the initial state area, calculating the final state area is non-trivial as dewetting effects frequently cause ink to separate into scattered depositions surrounding a substantially larger central deposition. Hence, basic pixel counting failed to analyze the spatial spread of the patterns and was not helpful for calculating drop shrinkage. To address that challenge, a convex hull^[23] was used to quantify the notional drop area for both states. However, due to the sensitivity of convex hulls to outliers, careful filtering of scattered satellite droplets was necessary prior to application. Thus, a filter that considers both particle size and spatial density was devised to determine which satellite drops belong to the core of the drop and which are outliers. First, satellite drops below 100 pixels in area were removed and considered insignificant. Next, core drops were defined as drops with centroids within 100 pixels of two other centroids. Outlier drops were those that did not meet this criterion. A region properties routine was utilized to calculate the centroids of each satellite drop and create a matrix of all drop centroid positions. Next, a nearest neighbor algorithm was utilized to calculate the two nearest neighbors of each drop. Core and outlier drops were then labeled, and a convex hull about only the core drops was computed. Finally, the initial state area and the final state convex hull area were computed to quantify the change in drop area throughout the drying process. Image processing was completed using functions from scikit-image, NumPy, OpenCV, and SciPy.

Mathematical models

Droplet evaporation

Evaporation in air is driven by the difference between the saturated concentration at the air/liquid interface and the ambient value in the environment. For contact angles smaller than 90° , evaporative flux is highest at the droplet edge so that the dominant flow in the absence of temperature gradients is radially outward. Evaporation typically drives nonuniform cooling that generates recirculating Marangoni flows via surface tension gradients.^[11] For a pinned droplet of radius R with small contact angle θ in an axisymmetric system of coordinates r and z , the local height h is

$$h(r, t) = \frac{R^2 - r^2}{2R} \theta(t) \quad (1)$$

The evaporation flux for a quasi-steady, diffusion-dominated process is^[24]

$$J(r) = \frac{2}{\pi} \frac{D_{vap} \Delta c_v}{\sqrt{R^2 - r^2}} \quad (2)$$

where D_{vap} is the diffusivity of water vapor in air ($= 26 \times 10^{-6} \text{ m}^2 \text{ s}^{-1}$ at 25°C) and Δc_v is the water vapor concentration difference ($= 1.6 \times 10^{-2} \text{ kg m}^{-3}$ at a relative humidity of 30%) between the drop surface and the surrounding. The contact angle can be expressed as a function of time t as follows^[24]:

$$\theta(t) = \frac{16D_{vap} \Delta c_v}{\pi R^2 \rho} (t_e - t) \quad (3)$$

where t_e is the total evaporation time and ρ is the density.

CO₂-driven diffusiophoresis in a droplet

When a sessile water droplet is exposed to CO₂, some CO₂ dissolves, producing ions inside the drop by the equilibrium chemical reaction ($\text{CO}_2 + \text{H}_2\text{O} \leftrightarrow \text{H}^+ + \text{HCO}_3^-$). For a stationary, non-evaporating drop, the CO₂ and ion concentrations, c_c and c_i , are respectively governed by coupled diffusion–reaction equations given by^[21,25]

$$\frac{\partial c_c}{\partial t} = \nabla \cdot (D_c \nabla c_c) - (k_f c_c - k_b c_i^2) \quad (4a)$$

$$\frac{\partial c_i}{\partial t} = \nabla \cdot (D_i \nabla c_i) + (k_f c_c - k_b c_i^2) \quad (4b)$$

where D_c is the diffusivity of CO₂ in water ($= 1.9 \times 10^{-9} \text{ m}^2 \text{ s}^{-1}$) and D_i is the ambipolar diffusion coefficient of the ions ($D_i = 2D_+D_-/(D_+ + D_-) = 2.1 \times 10^{-9} \text{ m}^2 \text{ s}^{-1}$), where $D_+ = 9.311 \times 10^{-9} \text{ m}^2 \text{ s}^{-1}$ and $D_- = 1.185 \times 10^{-9} \text{ m}^2 \text{ s}^{-1}$ are the cation and anion diffusivities, respectively. The forward and backward reaction rates are $k_f = 0.039 \text{ s}^{-1}$ and $k_b = 9.2 \text{ M}^{-1} \text{ s}^{-1}$, respectively. At the gas/liquid interface, the saturated CO₂ concentration is $c_{c,s} = p_{\text{CO}_2}/K_h = 0.034 \text{ M}$ where p_{CO_2} is the partial pressure of CO₂ ($= 1 \text{ atm}$) and K_h is the Henry law constant of CO₂ ($= 29.4 \text{ atmM}^{-1}$). The saturated ion concentration $c_{i,s}$ can be calculated as $c_{i,s} = 1.2 \times 10^{-4} \text{ M}$ with the assumption of local chemical equilibrium ($k_f c_{c,s} - k_b c_{i,s}^2 = 0$). Initial CO₂ and ion concentrations in the drop are calculated at $p_{\text{CO}_2} = 4 \times 10^{-4} \text{ atm}$, and are $c_{c,i} = 1.3 \times 10^{-5} \text{ M}$ and $c_{i,i} = 2.4 \times 10^{-6} \text{ M}$, respectively. Ion concentration gradients drive particle motion via diffusiophoresis at a velocity of

$$\mathbf{u}_{dp} = \Gamma_p \nabla \ln c_i \quad (5)$$

where Γ_p is the diffusiophoretic mobility. Finite Debye layer effects are considered because the Debye layer thickness to particle radius ratio $\lambda = (\kappa a)^{-1}$, where $\kappa^{-1} = \sqrt{\epsilon k_B T / 2Z^2 e^2 c_i}$ is approximately 0.078 for $1 \mu\text{m}$ diameter particles at $c_i = (c_{i,i} + c_{i,s})/2 \approx 0.06 \text{ mM}$. Thus, diffusiophoretic mobilities are^[15,26]

$$\Gamma_p = \frac{\epsilon}{\mu} \left(\frac{k_B T}{Ze} \right)^2 \left\{ \frac{Ze\zeta\beta}{k_B T} g(\lambda) + 4 \ln \left[\cosh \left(\frac{Ze\zeta}{4k_B T} \right) \right] h(\lambda) \right\} \quad (6a)$$

$$g(\lambda) = \left\{ 1 - \frac{\lambda k_B T}{2Ze\zeta} \left[F_1 + \frac{\epsilon}{2\mu D_i} \left(\frac{k_B T}{Ze} \right)^2 (\beta F_4 + F_5) \right] \right\}^{-1} \quad (6b)$$

$$h(\lambda) = \left\{ 1 - \frac{\lambda}{8 \ln \cosh \left(\frac{Ze\zeta}{4k_B T} \right)} \left[F_0 + \frac{\epsilon}{2\mu D_i} \left(\frac{k_B T}{Ze} \right)^2 (F_2 + \beta F_3) \right] \right\}^{-1} \quad (6c)$$

where ϵ is the permittivity, μ is the dynamic viscosity, k_B is the Boltzmann constant, T is the temperature, Z is the ion valence ($z_+ = -z_- = 1$), e is the elementary charge, ζ is the zeta potential, and β is $(D_+ - D_-)/(D_+ + D_-)$ for a Z:Z electrolyte. The F_n functions depend on ζ and are calculated using curve fits^[27] based on values of Prieve et al.^[15] We use the mean ζ measured at $c_i = c_{i,s}$ and $c_i = c_{i,i}$, where $\zeta = (42 + 20)/2 = 31 \text{ mV}$, which corresponds to $\Gamma_p \approx 0.3 \times 10^{-9} \text{ m}^2 \text{ s}^{-1}$ for aPS particles. Previous work has shown that the zeta potential change is negligible for a pH range of 3–9.^[28] We observed the pH of our particle solution to be within that range when CO₂ gas was pumped continuously for 5 min. Furthermore, the Debye layer thickness is primarily determined by ionic strength c_i of the solution, as can be seen in the equation $\kappa^{-1} = \sqrt{\epsilon k_B T / 2Z^2 e^2 c_i}$. Hence, the effect of pH variations on the surface charge and Debye layer thickness was considered to be negligible for our system.

Simulations

Simulations were performed with COMSOL Multi-physics 5.4a (COMSOL, Inc., USA). We considered the evaporation of an axisymmetric water droplet of 1 mm radius with a pinned contact line and initial contact angle of 38° . The substrate thickness was 0.1 mm. The drop radius was smaller than the capillary length $l_c = \sqrt{\sigma/\rho g} = 2.7 \times 10^{-3} \text{ m}$ for water, where σ is the surface tension and g is the gravitational acceleration, so that gravity was neglected. We solved coupled flow, heat transfer, and diffusion problems, and solved individual particle trajectories. The arbitrary Lagrangian–Eulerian (ALE) moving mesh was utilized to track the interface, and 3191 elements were used for the droplet where free triangular meshes were created with maximum element size of $15 \mu\text{m}$, and four boundary layers were used at the interfaces. The simulations were conducted using a parallel direct sparse solver (PARDISO) with a tolerance of 0.01.

Governing equations

The fluid dynamics are governed by the continuity and Navier–Stokes equations:

$$\nabla \cdot \mathbf{u} = 0 \quad (7)$$

$$\rho \left[\frac{\partial \mathbf{u}}{\partial t} + (\mathbf{u} \cdot \nabla) \mathbf{u} \right] = -\nabla p + \nabla \cdot (\mu \nabla \mathbf{u}) \quad (8)$$

where \mathbf{u} is the velocity vector, and p is the pressure. Heat transfer is governed by

$$\rho C_p \left(\frac{\partial T}{\partial t} + \mathbf{u} \cdot \nabla T \right) = \nabla \cdot (k \nabla T) \quad (9)$$

where C_p is the heat capacity, and k is the thermal conductivity. Species transport in the drop is governed by

$$\frac{\partial c}{\partial t} + \mathbf{u} \cdot \nabla c = \nabla \cdot (D \nabla c) + R_c \quad (10)$$

where c is the concentration, D is the diffusivity, and R_c is the reaction rate. Note, this form is used for evaporating drops such that convection is included [cf. Eqs. (4a) and (4b)]. Particle trajectories are governed by $d(m_p \mathbf{v})/dt = \mathbf{F}_D$ where m_p and \mathbf{v} are the mass and velocity of the particle, respectively, and \mathbf{F}_D is the drag force. Based on Stokes' law, $\mathbf{F}_D = 18\mu m_p (\mathbf{u}_t - \mathbf{v}) / \rho_p d_p^2$ where ρ_p is the particle density ($= 1000 \text{ kg m}^{-3}$), d_p is the particle diameter ($= 1 \mu\text{m}$), and \mathbf{u}_t is the sum of the fluid and diffusiophoretic velocities. Gravity, Brownian forces and particle-particle interactions are neglected.

For boundary conditions at the substrate ($z = 0$), no slip is applied for the fluid flow and no-flux conditions are applied for all species. A temperature of $T_s = 298 \text{ K}$ is applied to the bottom of the substrate ($z = -0.1 \text{ mm}$), and no-flux conditions are used for the remaining substrate surfaces. At the droplet surface, $\mathbf{u} \cdot \mathbf{n} = 0$, $k \nabla T \cdot \mathbf{n} = -J(r) h_l$ where h_l is the latent heat of vaporization, and $(\mathbf{n} \cdot \boldsymbol{\tau}_l) \cdot \mathbf{t} = d\sigma/dT (\nabla T \cdot \mathbf{t})$ which drives Marangoni flows. Here, \mathbf{t} is the unit tangent vector to the surface and $\boldsymbol{\tau}_l$ is the viscous stress tensor. For concentrations, $c = c_{i,s}$ and $c = c_{c,s}$ for ion and CO_2 , respectively. Equation (2) is used for the evaporative flux, and Eq. (1) is used to impose the movement of the droplet surface. Here, $D_{vap} = 26 \times 10^{-6} \text{ m}^2 \text{ s}^{-1}$ for the ambient air in N_2 and $D_{vap} = 15 \times 10^{-6} \text{ m}^2 \text{ s}^{-1}$ in CO_2 . Zero mesh displacement in both the r and z -directions are used at the droplet's base radius, preventing movement of the contact line during evaporation. For particles, bounce wall conditions are applied at the substrate and droplet interface ($\mathbf{v} = \mathbf{v}_c - 2(\mathbf{n} \cdot \mathbf{v}_c)\mathbf{n}$, where \mathbf{v}_c is the particle velocity when striking the boundary).

Results and discussion

Simulations

As a proof of concept, we first simulate the motion of positively charged aPS particles ($\zeta \approx 31 \text{ mV}$) in a stationary, non-evaporating drop. Figure 2(a)(i) shows the resulting ion gradient in the drop and the associated particle migration toward the drop interface. Figure 2(a)(ii) shows the typical flow profile in an evaporating drop at 30% relative humidity at $t = 10 \text{ s}$. The primary flow is toward the droplet edge where the evaporation flux is highest. Figure 2(a)(iii) shows the flow profile, including Marangoni effects, where the surface tension gradients

drive rotating internal flow. Velocities associated with Marangoni flows ($O(0) - O(1) \text{ mms}^{-1}$) are faster than those for pure evaporation ($O(0) - O(10) \mu\text{ms}^{-1}$). Particle dynamics are calculated for various conditions in Fig. 2(b) at 2, 4, 6, 10, and 20 s. Figure 2(b)(i) shows the particle dynamics in an evaporating drop in air with Marangoni effects. Here, particles are convecting along the rotating Marangoni flows and are prevented from accumulating at the contact line over this time scale. Figure 2(b)(ii) shows the results for evaporation in CO_2 , including diffusiophoresis. As seen, the Marangoni flow drives a swirling behavior of the dissolved ion concentration, which complicates the role of diffusiophoresis, as the particles move toward high concentration. In these conditions, the Marangoni flow tends to dominate the effects of diffusiophoresis, except near the substrate, where the fluid velocity is necessarily low, which allows diffusiophoresis to still drive particles along the substrate toward the contact line. However, the strong mixing via Marangoni flows leads to nearly saturated ion concentrations within 10 s, such that diffusiophoretic effects are not long lived. Finally, Fig. 2(b)(iii) shows the particle dynamics in CO_2 without Marangoni effects, in which diffusiophoresis is able to drive significant particle motion toward the interface, and the ion gradients can persist for a significantly longer timescale.

Figure 2(c) shows the evolution of the ion concentration profile along the r -direction at $t = 2, 4, 6,$ and 10 s in an evaporating droplet in CO_2 at a height of $2 \mu\text{m}$ from the substrate surface. At early times, the high ion concentration region is confined near the interface, where it is pulled radially inward along the interface by the Marangoni flows, leading to relatively fast saturation near the center. The ion concentration appears to fully saturate in around 10 s. Figure 2(d) shows the diffusiophoretic velocity of the aPS particles in the r -direction based on the calculated concentration profiles of Fig. 2(c) with the diffusiophoretic mobility of $0.3 \times 10^{-9} \text{ m}^2 \text{ s}^{-1}$. Since aPS particles are driven toward higher concentrations by diffusiophoresis, their migration direction changes at $r \approx 0.45 \text{ mm}$ at $t = 2 \text{ s}$, again due to the recirculating Marangoni flow. Here, the maximum velocity of the particles is about $2.5 \mu\text{ms}^{-1}$ at $r \approx 0.8 \text{ mm}$. At $t = 4 \text{ s}$, the diffusiophoretic particle transport is driven toward the contact line at $r > \sim 0.8 \text{ mm}$ as the radial position with the lowest concentration value moves, where the maximum velocity is $\sim 1.7 \mu\text{ms}^{-1}$. The diffusiophoresis decays over approximately 10 s due to the concentration saturation. Figure 2(e) shows the relative fluid velocity magnitudes both with and without Marangoni effects in CO_2 at a height of $2 \mu\text{m}$ from the substrate. Magnitudes with Marangoni effects are significantly stronger, but both diverge near the contact line due to the diverging evaporative flux. These results indicate that diffusiophoresis is relatively weak compared to the fluid flow, including Marangoni effects, although diffusiophoresis can dominate the fluid flow without Marangoni effects over the early time regime. Nevertheless, our experiments show a significant difference in the particle depositions with and without diffusiophoresis. This is likely due to the fact that

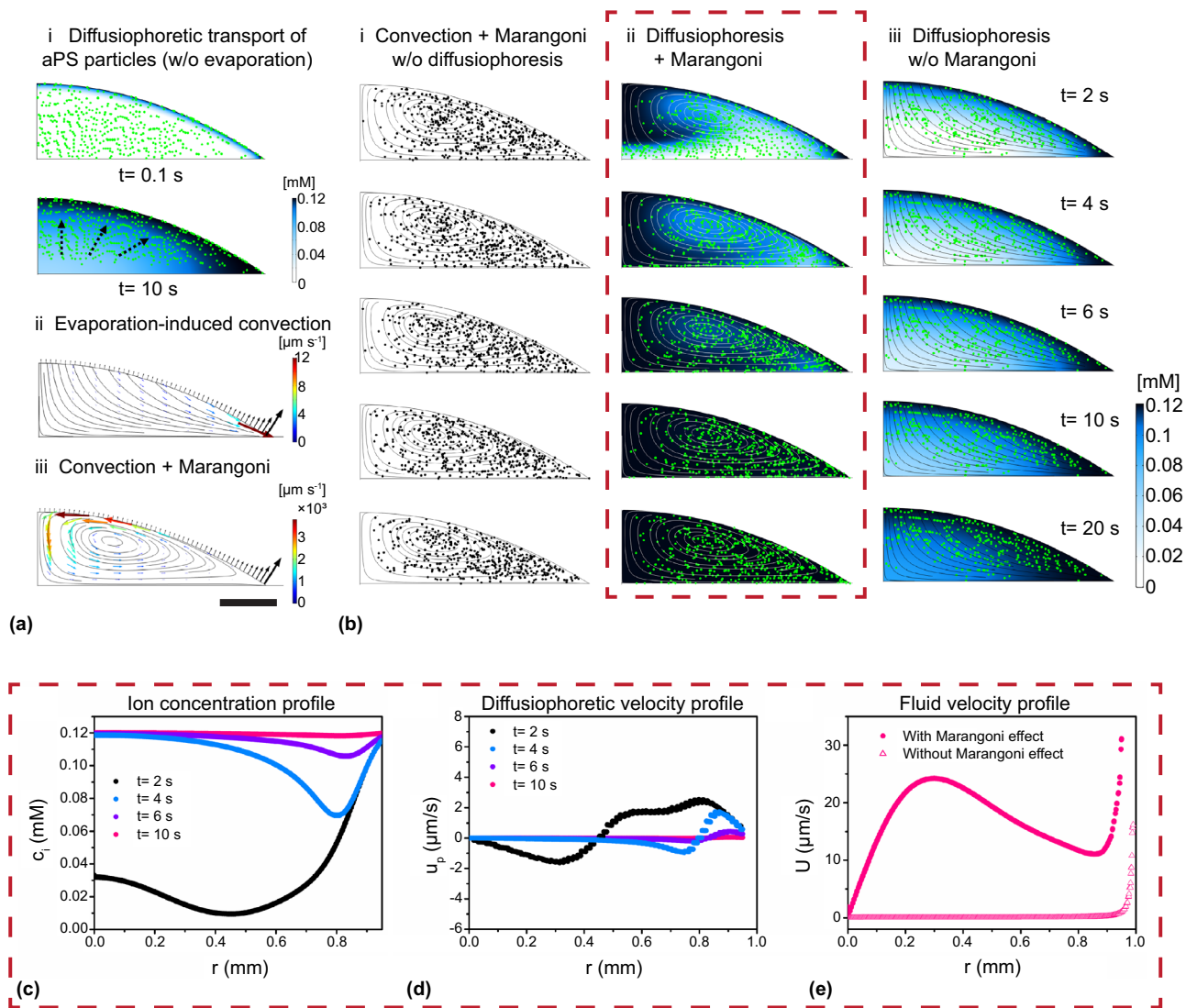


Figure 2. Simulation results of the fluid/particle dynamics in a drying drop. (a) (i) Diffusiophoretic transport of positively charged aPS particles in a stationary drop without evaporation. Streamlines and velocities (arrows) of (ii) evaporation-induced convection flows and (iii) Marangoni flows coupled with convection in air at $t = 10$ s. (b) Particle transport in the evaporating drops at $t = 2, 4, 6, 10$ and 20 s for (i) evaporation in air (without diffusiophoresis), (ii) evaporation in a CO_2 environment (with diffusiophoresis), and (iii) evaporation without Marangoni flows in CO_2 . Particles have $1 \mu\text{m}$ diameters and are scaled by $10 \times$ in these images. (c) Ion concentrations and (d) diffusiophoretic velocities in the drop in CO_2 at $t = 2, 4, 6$ and 10 s. (e) Fluid velocity near the substrate with and without Marangoni effects in CO_2 at $t = 10$ s. Results in (c–e) are calculated at $2 \mu\text{m}$ from the substrate surface. The dashed box around c–e highlights the background conditions in (b) (ii) for which the profiles are calculated. The scale bar is $250 \mu\text{m}$.

diffusiophoresis can still dominate the Marangoni flows near the substrate because of no-slip, which allows particle motion toward the contact line near the substrate and can also alter the pinning dynamics of the contact line.

As noted, the droplet radii in the experiments are approximately 1.2 and 1 mm in the simulations. One consequence of this difference is that the diffusive/diffusiophoretic processes will persist approximately 44% longer in the experiments, since their timescales scale like a^2/D_i and a^2/Γ_p , respectively. Thus, the simulations may underpredict the diffusiophoresis/diffusiophoresis. The evaporation flux [Eq. (2)] and Marangoni

effects also depend on size. However, for 1 and 1.2 mm radii, the average velocities of the convection flows are comparable, which are $9.8 \times 10^{-7} \text{ms}^{-1}$ and $8.2 \times 10^{-7} \text{ms}^{-1}$, respectively, and the average velocities from Marangoni effects are $3.4 \times 10^{-4} \text{ms}^{-1}$ and $3.7 \times 10^{-4} \text{ms}^{-1}$, respectively. Here, the purpose of the simulations is not to make a one-to-one quantitative comparison with the experimental pattern depositions, which would require more sophisticated simulations, including the finite particle size and an adhesion model, but rather to gain insights into the relative balance of the physics and understand the transport. Given the relatively similar magnitudes of the

different transport processes mentioned above, these droplet sizes are sufficiently similar for our purposes.

Experiments

As proof of concept, we performed experiments of the evaporative-driven assembly in both N_2 and CO_2 environments. Figure 3 shows the results for the final dried patterns in both conditions. In N_2 , the drops evaporate in ambient conditions without diffusiophoresis. Here, a complex interplay of forces, such as capillary and Marangoni flow effects, guide the evaporation^[29]. Figure 3(i–iii) shows the formation of a clustered deposit with scattered dewetting patterns around it. This suggests that the pinning force is insufficient to pin the droplet, and dewetting occurs.^[29] As the droplet continuously depins, leaving scattered deposits, the droplet volume decreases and ultimately deposits as a clustered feature. These patterns are guided by the print parameters such as particle concentration and substrate, and the N_2 does not play a role. N_2 is inert and does not dissociate to form ions in aqueous solvents. These experiments serve as controls for comparison with droplets printed in other environments. The real-time evaporation process of aPS particles in N_2 is shown in the video (Online Resource 1). Figure 3(iv–vi) shows the printed patterns in a CO_2 environment, exhibiting a relatively uniform internal texture with a strong peripheral coffee ring.^[30] We attribute this pattern variation to the introduction of diffusiophoresis. The CO_2 produces non-interfering solute ions in the drop yielding transient concentration gradients that drive particle diffusiophoresis. In this case, the diffusiophoresis alters the particle dynamics near the substrate and contact line in such a manner as to increase the pinning forces enough to fix the contact line and produce a relatively

uniform internal texture. The real-time evaporation process of aPS particles in CO_2 is shown in the video (Online Resource 2).

Quantitative comparisons of the drying behavior were performed leveraging image-processing techniques. Figure 4 highlights the significant real-time variation in pattern and size for droplets dried under CO_2 and N_2 . Figure 4(a) shows the image-processing workflow, which uses knowledge from our earlier work^[30] to segment the printed samples. As described earlier in Sect. “Image analysis,” the calculation of the drop area was trivial for the initial state as all ink remained coalesced into a single drop. Thus, simple pixel counting of the initial state segmentation was sufficient. However, a similar pixel-counting approach for the final state image failed to provide an area estimate of the spatial spread of the pattern and, hence, was inaccurate to characterize the drying behavior of the droplet. To address this challenge, the convex hull approach was used. The convex hull is a useful tool for estimating the smallest convex boundary that contains all the points of interest. This approach was relatively accurate in predicting the drop boundary containing the isolated deposits, hence, providing a more precise drop area. Leveraging this, we successfully estimated the boundary of the drying droplets, and the drop areas of initial and final states were then compared to quantify the degree of shrinkage.

Real-time images of the deposition processes in N_2 and CO_2 are shown in Fig. 4(b), (c) at 0, 300, 600, 900, 1200 s, and at complete evaporation. At 300 s, particles exhibit stronger motion toward the contact line in CO_2 , contributing to the thicker ring-like pattern. At 600 s, the contact line has begun slipping in N_2 , unlike the pattern in CO_2 , where the pinning is strong, and the particles begin to deposit a ring-like pattern. This is illustrated by the segmented area in N_2 , which has

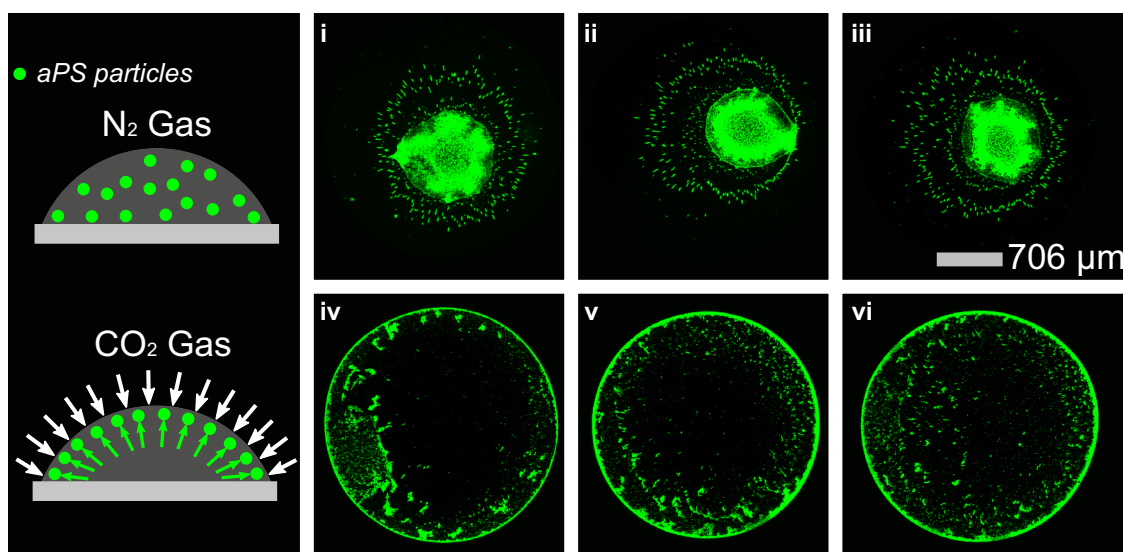


Figure 3. (Left) Illustrations of the diffusiophoretic effects on evaporative assembly of positively charged amine-modified polystyrene (aPS) particles exposed to gaseous environments of nitrogen and carbon dioxide, respectively. Experimentally observed colloidal patterns in the presence of N_2 gas are shown in (i–iii) and those in CO_2 are shown in (iv–vi).

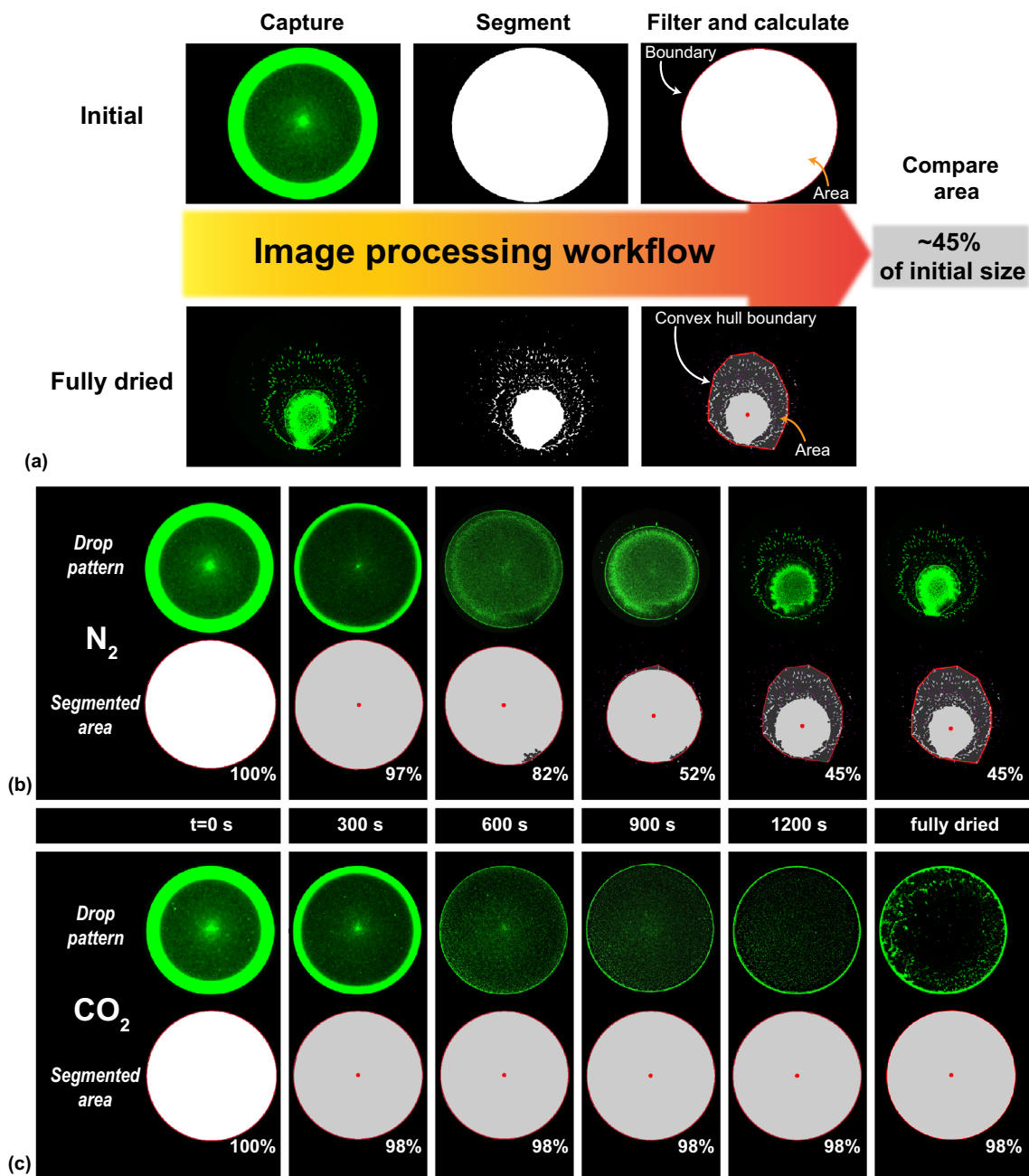


Figure 4. (a) Image processing workflow to calculate shrinkage ratios of the dried patterns, compared to their initial print sizes. The convex hull area is calculated for the droplets from the real-time images at the start of the print and at complete evaporation. Time-lapse images of a representative droplet along with the processed convex hull boundary are shown as the droplet evaporates in (b) N_2 and (c) CO_2 environments at $t=0$, 300, 600, 900, 1200 s and at complete evaporation. The ‘segmented area’ highlights the droplet area at each instant, compared to the initial droplet area.

reduced to 82% of its initial size. This continues as the droplet dries, and at 1200 s, scattered dewetting drops become prominent in N_2 , with the area decreasing to 45%, while in CO_2 , the drop size remains fairly constant with an increase in ring thickness. Although the drop sizes shrink to almost half the initial size in exposure to N_2 , the deposition patterns in CO_2 demonstrate relatively constant areas throughout the evaporation

with variations of only about 2%. Nevertheless, the convex hull approach is susceptible to overestimating the non-convex shapes, such as the scattered droplets. Hence, it is not entirely accurate in calculating drop area and introduces some variation in the measurements. Such variations in area measurements can be further improved by tweaking the filtering process to detect lower-intensity scattered deposits of significant size.

Conclusions

In this paper, we demonstrated that diffusiophoresis can alter the evaporation dynamics and provide a new mechanism for controlling particle deposition and pattern formation in drying drops simply by modulating the microenvironment. We performed simulations of the particle dynamics in a variety of scenarios, including with and without evaporation, Marangoni effects, and diffusiophoresis. Results show that Marangoni effects typically dominate the particle motion, but diffusiophoresis may play a role near the substrate and near the contact line. Next, we fabricated a customized microenvironment chamber for microextrusion printing with *in-situ* fluorescence imaging and observed the drying dynamics and pattern formation for evaporating drops in N₂ and CO₂ environments. Image analysis was performed to quantify the area shrinkage of the printed patterns for both cases. These results address the critical scientific gaps on whether gas-based, non-contaminating solutes can generate sufficient forces to affect the pattern formation process in the evaporative assembly of colloidal particles. Future work can involve exploring other particles and gas combinations to gain a better insight into the complex patterning process. Ultimately, we envision that the incorporation of diffusiophoresis can enable a fundamentally new and versatile control of particle deposition in a multi-scale AM process. Further, future integration of our system with advanced computer vision and ML tools for classifying and characterizing the printed droplets can enable automated, high-throughput AM of electronics and functional devices.

Funding

Y.L.K. acknowledges the support from the National Institutes of Health (NIH) NIBIB Trailblazer Award (Grant No. R21-EB029563); NIH NIBIB R01 Award (Grant No. R01-EB032959); Office of Naval Research Young Investigator Program Award (ONR YIP), 3M Non-Tenured Faculty Award; CDMRP Discovery Award, National Science Foundation (NSF) under Emerging Frontiers in Research and Innovation (EFRI) Program (Grant No. EFRI 1830958) and the Utah NASA Space Grant Consortium Faculty Research Seed Funding Awards. J.L. thanks the National Research Foundation of Korea (NRF) grant funded by the Ministry of Science, ICT & Future Planning, and the Ministry of Education (NRF2020R1A2C3010568 and NRF2021R1A6A1A03039696). J.A. thanks the Brown School of Engineering for funding. M.J. and S.R.K. acknowledge support from Vannevar Bush Fellowship with Office of Naval Research (ONR) Grant #N00014-18-1-2879.

Data availability

The data that support the findings of this study are available upon reasonable request from the authors.

Declarations

Conflict of interest

Y.L.K. is an inventor on multiple active patents describing 3D-printing technologies, including active electronic materials and devices and multifunctional hybrid devices and structures. Y.L.K. is also an inventor of gastric-resident systems, including gastric-resident electronics. All other authors declare no conflict of interest.

Supplementary Information

The online version contains supplementary material available at <https://doi.org/10.1557/s43579-023-00432-4>.

References

1. D. Kokkinis, M. Schaffner, A.R. Studart, Multimaterial magnetically assisted 3D printing of composite materials. *Nat Commun.* **6**, 8643 (2015)
2. Y.L. Kong, I.A. Tamargo, H. Kim, B.N. Johnson, M.K. Gupta, T.-W. Koh, H.-A. Chin, D.A. Steingart, B.P. Rand, M.C. McAlpine, 3D printed quantum dot light-emitting diodes. *Nano Lett.* **14**, 7017–7023 (2014)
3. Q. Zhang, F. Zhang, X. Xu, C. Zhou, D. Lin, Three-dimensional printing hollow polymer template-mediated graphene lattices with tailorable architectures and multifunctional properties. *ACS Nano* **12**, 1096–1106 (2018)
4. B. Elder, R. Neupane, E. Tokita, U. Ghosh, S. Hales, Y.L. Kong, Nanomaterial patterning in 3D printing. *Adv. Mater.* **32**, 1907142 (2020)
5. N. Bassik, G.M. Stern, M. Jamal, D.H. Gracias, Patterning thin film mechanical properties to drive assembly of complex 3D structures. *Adv. Mater.* **20**, 4760–4764 (2008)
6. A.T.L. Tan, J. Beroz, M. Kolle, A.J. Hart, Direct-write freeform colloidal assembly. *Adv. Mater.* **30**, 1803620 (2018)
7. T.P. Bigioni, X.-M. Lin, T.T. Nguyen, E.I. Corwin, T.A. Witten, H.M. Jaeger, Kinetically driven self assembly of highly ordered nanoparticle monolayers. *Nat. Mater.* **5**, 265–270 (2006)
8. R.D. Deegan, O. Bakajin, T.F. Dupont, G. Huber, S.R. Nagel, T.A. Witten, Capillary flow as the cause of ring stains from dried liquid drops. *Nature* **389**, 827–829 (1997)
9. A. Askounis, K. Sefiane, V. Koutsos, M.E.R. Shanahan, The effect of evaporation kinetics on nanoparticle structuring within contact line deposits of volatile drops. *Colloids. Surf. A Physicochem. Eng. Asp.* **441**, 855–866 (2014)
10. D.J. Harris, J.A. Lewis, Marangoni effects on evaporative lithographic patterning of colloidal films. *Langmuir* **24**, 3681–3685 (2008)
11. H. Hu, R.G. Larson, Marangoni effect reverses coffee-ring depositions. *J. Phys. Chem. B* **110**, 7090–7094 (2006)
12. B.V. Derjaguin, G. Sidorenkov, E. Zubashchenko, E. Kiseleva, Kinetic phenomena in the boundary layers of liquids 1: the capillary osmosis. *Prog. Surf. Sci.* **43**, 138–152 (1993)
13. B.V. Derjaguin, S.S. Dukhin, A.A. Korotkova, Diffusiophoresis in electrolyte solutions and its role in the Mechanism of the formation of films from caoutchouc latexes by the ionic deposition method. *Prog. Surf. Sci.* **43**, 153–158 (1993)
14. J.L. Anderson, M.E. Lowell, D.C. Prieve, Motion of a particle generated by chemical gradients part 1: non-electrolytes. *J. Fluid Mech.* **117**, 107–121 (1982)
15. D.C. Prieve, J.L. Anderson, J.P. Ebel, M.E. Lowell, Motion of a particle generated by chemical gradients: part 2—electrolytes. *J. Fluid Mech.* **148**, 247–269 (1984)
16. J. Anderson, Colloid transport by interfacial forces. *Annu. Rev. Fluid Mech.* **21**, 61–99 (1989)
17. S. Shin, E. Um, B. Sabass, J.T. Ault, M. Rahimi, P.B. Warren, H.A. Stone, Size-dependent control of colloid transport via solute gradients in dead-end channels. *Proc. Natl. Acad. Sci.* **113**, 257–261 (2016)

18. J.T. Ault, P.B. Warren, S. Shin, H.A. Stone, Diffusiophoresis in one-dimensional solute gradients. *Soft Matter* **13**, 9015–9023 (2017)
19. J. Palacci, B. Abécassis, C. Cottin-Bizonne, C. Ybert, L. Bocquet, Colloidal motility and pattern formation under rectified diffusiophoresis. *Phys. Rev. Lett.* **104**, 138302 (2010)
20. J. Palacci, C. Cottin-Bizonne, C. Ybert, L. Bocquet, Osmotic traps for colloids and macromolecules based on logarithmic sensing in salt taxis. *Soft Matter* **8**, 980–994 (2011)
21. S. Shin, O. Shardt, P.B. Warren, H.A. Stone, Membraneless water filtration using CO₂. *Nat. Commun.* **8**, 15181 (2017)
22. T.J. Shimokusu, V.G. Maybruck, J.T. Ault, S. Shin, Colloid separation by CO₂-induced diffusiophoresis. *Langmuir* **36**, 7032–7038 (2020)
23. M Goyal, Morphological image processing. *IJCST* **2** (2011)
24. Á.G. Marín, H. Gelderblom, D. Lohse, J.H. Snoeijer, Order-to-disorder transition in ring-shaped colloidal stains. *Phys. Rev. Lett.* **107**, 085502 (2011)
25. S. Shim, S. Khodaparast, C.-Y. Lai, J. Yan, J.T. Ault, B. Rallabandi, O. Shardt, H.A. Stone, CO₂-driven diffusiophoresis for maintaining a bacteria-free surface. *Soft Matter* **17**, 2568–2576 (2021)
26. S. Shin, Diffusiophoretic separation of colloids in microfluidic flows. *Phys. Fluids* **32**, 101302 (2020)
27. S. Lee, J. Lee, J.T. Ault, The role of variable zeta potential on diffusiophoretic and diffusioosmotic transport. *Colloids Surf. A Physicochem. Eng. Asp.* **659**, 130775 (2023)
28. S. Shim, J.K. Nunes, G. Chen, H.A. Stone, Diffusiophoresis in the presence of a pH gradient. *Phys. Rev. Fluids* **7**, 110513 (2022)
29. W. Li, D. Lan, Y. Wang, Dewetting-mediated pattern formation inside the coffee ring. *Phys. Rev. E* **95**, 042607 (2017)
30. R.D. Deegan, Pattern formation in drying drops. *Phys. Rev. E* **61**, 475–485 (2000)

Publisher's Note Springer Nature remains neutral with regard to jurisdictional claims in published maps and institutional affiliations.

Springer Nature or its licensor (e.g. a society or other partner) holds exclusive rights to this article under a publishing agreement with the author(s) or other rightsholder(s); author self-archiving of the accepted manuscript version of this article is solely governed by the terms of such publishing agreement and applicable law.